LAWRENCE
LIVERMORE
NATIONAL
LABORATORY

LLNL-PROC-497352

HRTEM Study of the Role of Nanoparticles in ODS Ferritic Steel

L. Hsiung, S. Tumey, M. Fluss, Y. Serruys, F. Willaime

September 1, 2011

2010 MRS Fall Meeting
Boston, MA, United States
November 28, 2010 through December 3, 2010

Disclaimer

HRTEM Study of the Role of Nanoparticles in ODS Ferritic Steel under Dual-Ion Irradiation

Luke Hsiung[1*], Scott Tumey[1], Michael Fluss[1], Yves Serruys[2], and Francois Willaime[2]

[1]Lawrence Livermore National Laboratory
Physical and Life Sciences Directorate
Livermore, CA94551, U.S.A.
[2]Service de Recherches de Métallurgie Physique (CEA)
Gif-sur-Yvette 91191, France

ABSTRACT

Structures of nanoparticles and their role in dual-ion irradiated Fe-16Cr-4.5Al-0.3Ti-2W-0.37Y_2O_3 (K3) ODS ferritic steel produced by mechanical alloying (MA) were studied using high-resolution transmission electron microscopy (HRTEM) techniques. The observation of $Y_4Al_2O_9$ complex-oxide nanoparticles in the ODS steel imply that decomposition of Y_2O_3 in association with internal oxidation of Al occurred during mechanical alloying. HRTEM observations of crystalline and partially crystalline nanoparticles larger than ~2 nm and amorphous cluster-domains smaller than ~2 nm provide an insight into the formation mechanism of nanoparticles/clusters in MA/ODS steels, which we believe involves solid-state amorphization and re-crystallization. The role of nanoparticles/clusters in suppressing radiation-induced swelling is revealed through TEM examinations of cavity distributions in (Fe + He) dual-ion irradiated K3-ODS steel. HRTEM observations of helium-filled cavities (helium bubbles) preferably trapped at nanoparticle/clusters in dual-ion irradiated K3-ODS are presented.

INTRODUCTION

One of the major challenges in designing future fusion reactors is to develop the high-performance structural materials for first wall and diverter components, which will be exposed high-energy neutrons (14 MeV) from the deuterium-tritium fusion and helium (He) and hydrogen (H) from in (α, n)- and (n, p)-transmutation reactions [1]. The choice of structural materials dictates the design of the fusion reactor systems. In particular, the allowable power plant operating temperature, the choice of coolant, and the power conversion system are critically dependent on the performance characteristics of the materials. Oxide dispersion strengthened (ODS) steels, which produced by mechanical alloying of the elemental (or pre-alloyed) metallic powder with yttria (Y_2O_3) oxide powder and consolidated by hot extrusion or hot isostatic pressing, are a class of advanced structural materials with a potential to be used at elevated temperatures due to the dispersion of thermally stable oxide nanoparticles into the matrix. ODS steels are resistant to radiation-induced swelling and have improved creep strength and oxidation/corrosion resistance at elevated temperatures compared to conventional steels. Thus an operating temperature of the first wall in future fusion of > 700 ºC [2] is possible, resulting in an improved efficiency of ≥ 40% [3].

Since no prototype fusion reactors currently exist, it is difficult to directly evaluate the effects of high-energy neutron and transmutation gases on the first wall and diverter components of a

* Corresponding author. Tel.: +1-925 424 3125; fax: +1-925 424 3815
E-mail address: hsiung1@llnl.gov (Luke L. Hsiung).

fusion reactor. One technique commonly used to study the evolution of defect structures and the kinetics of cavity formation utilizes transmission electron microscopy (TEM) examinations of specimens simultaneously bombarded by heavy ions and helium and/or deuterium ions through so called "dual-beam" and "triple-beam" accelerated experiments [4, 5]. The heavy ions create atomic displacements while the gas ions result in the effects of the transmutation gases, helium (10 appm/dpa) and hydrogen (40 ~ 45 appm/dpa) [1, 6]. In preparation for the "dual-beam" and "triple-beam" experiments, we have conducted HRTEM characterization of as-fabricated Fe-16Cr ODS steel with alloying additions of Al and Ti to document crystal structure, density population, size distribution, and interfacial structure of oxide nanoparticles. Emphasis was placed on studying the formation mechanism of nanoparticles that are crucial in trapping helium bubbles to suppress radiation-induced cavitational swelling.

EXPERIMENTAL

The ODS steel used for this investigation was Fe-16Cr-4Al-2W-0.3Ti-0.3Y_2O_3 (designated as K3 [7]) ODS ferritic steel. A full description of the fabrication procedure for the ODS steels can be found elsewhere [8, 9]. Briefly, the pre-alloyed powder was first mechanically alloyed with Y_2O_3 powder in an argon gas atmosphere at room temperature using an attrition-type ball mill. The powder was then sealed in a stainless-steel can and degassed at 400 °C in 0.1 Pa pressure. The canned powders were subsequently consolidated by a hot extrusion technique at 1150 °C. After the extrusion, the consolidated K3-ODS steel was thermally treated at 1050 °C for 1 hour. One sample of K3-ODS steel was also annealed at 900 °C for 168 h (one week) for a thermal-stability study. The chemical composition (in wt.%) of the two ODS steels are: C: 0.08, Si: 0.033, Cr: 16, W: 1.82, Al: 4.59, Ti: 0.28, Y_2O_3: 0.368, and Fe: balance [7]. Dual-beam irradiation of K3-ODS steel loaded in a stainless-steel specimen holder using 24.18 MeV Fe^{8+} ions for displacement damage and energy-degraded 1.7 MeV He^+ ions for helium injection was conducted at the JANNUS facility, Saclay, France. The irradiation temperature was controlled at 425 ± 5 ^oC using a PID referenced thermocouple located on the specimen holder. The specimen temperature uniformity was estimated by monitoring the surface temperature of the specimen using a digital infrared camera during heating and ion irradiation. The surface temperature was uniform within ± 2.5 ^oC and tracked well with the controlling thermocouple. Figure 1 shows the calculated profiles of displacement damage (dpa), Fe^{8+}, and He^+ using TRIM code. The implantation depth of helium was over a region extending from 1.5 to 2.75 μm beneath the specimen surface to avoid overlapping with the Fe^{8+} ion region that was over a region extending from 2.75 to 3.6 μm beneath the specimen surface. The displacement damage at the peak position was 65 dpa, and the specimens were irradiated at ~1 x 10^{-3} dpa/s. The nominal conditions for ion irradiation at the helium implantation region are as follows: the displacement damage gradually increases from 10 dpa (at 1.5 μm) to 40 dpa (at 2.75 μm), and there are two peaks for helium to dpa ratio within the helium implantation region: 100 appm/dpa at 2.1 μm and 25 appm/dpa at 2.6 μm. Thin foils for TEM examination were prepared by a standard procedure that includes slicing, grinding, and polishing. Final thinning of the foils was performed using a standard twin-jet electropolishing technique in an electrolyte (90 vol.% acetic acid, 10 vol.% perchloric acid) at 30 V and room temperature. TEM foils (10 μm x 6 μm x < 0.1 μm) of irradiated K3-ODS were prepared using a focused ion-beam (FIB) method. The foils were lifted out using a micro pick-up system and mounted onto a copper grid. TEM characterizations were performed using a Phillips CM300 field-emission transmission electron microscope (accelerating voltage of 300 kV). A software package CaRIne Crystallography 3.1 [10] was used to simulate electron diffraction patterns to identify the crystal structure of oxide nanoparticles.

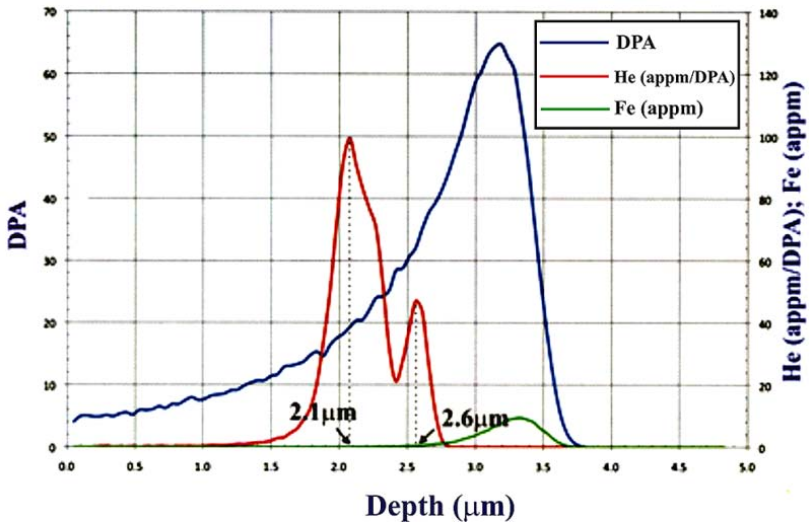

Fig. 1. TRIM calculation of dose (dpa), helium-to-dpa ratio (appm/dpa), and Fe (appm) profiles. The penetration depth of ions was over a region that extends from 1.5 to 2.75 μm beneath the specimen surface for He and extends from 2.75 to 3.6 μm beneath the specimen surface for Fe.

RESULTS AND DISCUSSION

Typical microstructures of K3 steel are shown in Fig. 2a-2b. Here elongated grains and oxide nanoparticles, mainly $Y_4Al_2O_9$ (YAM: Yttrium Aluminum Monoclinic) were observed. The number density and size distribution of oxide particles of K3-ODS steel were investigated using energy-filtered transmission electron microscopy (EFTEM) method. The results are shown in Figs. 3. The nanoparticle sizes in K3-ODS are typically ranging from 1.69 nm to 67.24 nm in diameter with a mean particle size: 5.91 nm and a particle density: 1.33×10^{22} m^{-3}. It is worth noting that this result may also indicate that the size limit of observable nanoparticles using energy-filtered electron microscopy is 1.7 nm. As we will demonstrate below, the smallest crystalline nanoparticles we observed by HRTEM are in the range of 1.7 to 2 nm. Particles or cluster-domains smaller than this, in our observations, were featureless or possibly amorphous in nature and were difficult to resolve using conventional TEM imaging techniques. $Y_4Al_2O_3$ (YAM) has a monoclinic structure (space group: $P2_1/c$) with lattice parameters: a = 0.7375 nm, b = 1.0507 nm, c = 1.1113 nm, and β = 108.58º [11, 12]. An orientation relationship between the $Y_4Al_2O_9$ oxide nanoparticle and the Fe-Cr (α) matrix can be derived from the diffraction pattern shown in Fig. 2a: $(0\bar{1}1)_\alpha \parallel (2\bar{4}2)_{YAM}$ and $[011]_\alpha \parallel [432]_{YAM}$. By comparing the $Y_4Al_2O_9$ nanoparticles formed in the ODS steel with the starting Y_2O_3 particles (space group: Ia_3, a cubic structure with a_o = 1.06 nm [11], particle size distribution: 15 – 50 nm [13]) used to fabricate the ODS steels, we can realize that the formation of oxide nanoparticles in ODS steels is not solely through fragmentation of Y_2O_3 particles. In fact, a more complex formation mechanism, which involves fragmentation of Y_2O_3 particles, decomposition/dissolution of Y_2O_3 fragments, and reprecipitation of nanoscale precipitates/clusters, has been proposed by Okuda and Fujiwara [14], Kimura et al. [15], Sakasegawa et al. [16], and Alinger et al. [17]. To form $Y_4Al_2O_9$ nanoparticles in consolidated MA/ODS steels, the following three reactions should also take place: 1) a dissolution of Y_2O_3 powder particles: $Y_2O_3 \rightarrow 2\,[Y] + 3\,[O]$, 2) an internal oxidation reaction of Al: $2\,[Al] + 3\,[O] \rightarrow Al_2O_3$ due to the higher oxygen-affinity of Al (i.e., Al > Ti > Cr > Fe [18]), and 3) a complex-oxide formation reaction: $2Y_2O_3 +$

$Al_2O_3 \rightarrow Y_4Al_2O_9$, which can take place at temperatures between 900 °C and 1100 °C [19]. Most recent studies of oxide nanoparticles in various ODS steels conducted by Marquis [20] using atom probe tomography (APT), Klimiankou et al. [21] using energy dispersive x-ray (EDX) and electron energy loss spectroscopy (EELS) analyses, and Hsiung et al. [22] using HRTEM revealed the existence of a core/shell structure in oxide nanoparticles. The findings of core/shell structures in oxide nanoparticles therefore suggest that the dissolution/reprecipitation mechanism previously proposed for the formation of oxide nanoparticles in as-fabricated ODS steels is not fully accountable.

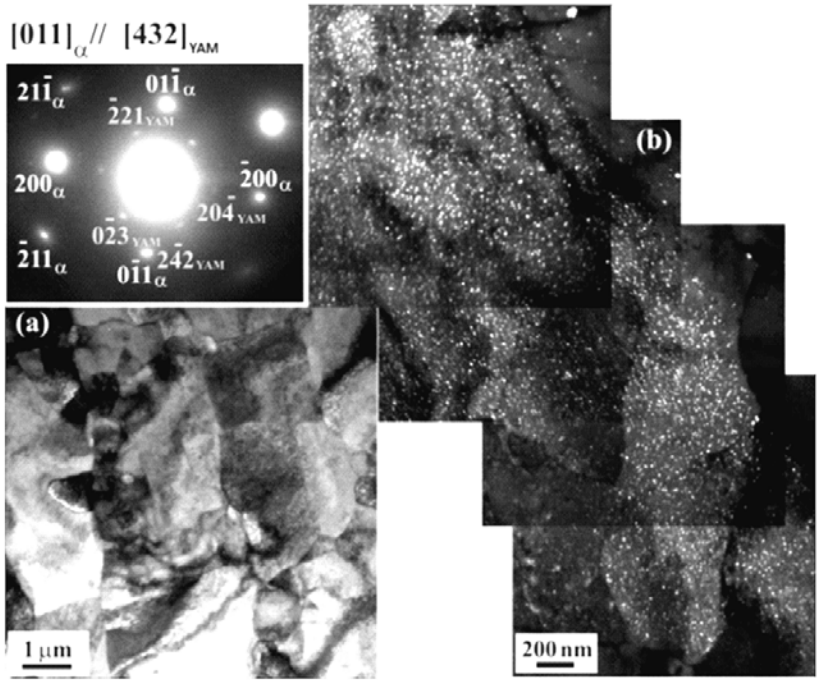

Fig. 2. (a) Bright-field TEM image shows typical grain morphology of K3-ODS steel, (b) dark-field TEM image and selected-area diffraction pattern of the $[011]_{Fe\text{-}Cr(\alpha)}$ || $[432]_{YAM}$-zone show the formation of dense $Y_4Al_2O_9$ nanoparticles in K3-ODS steel.

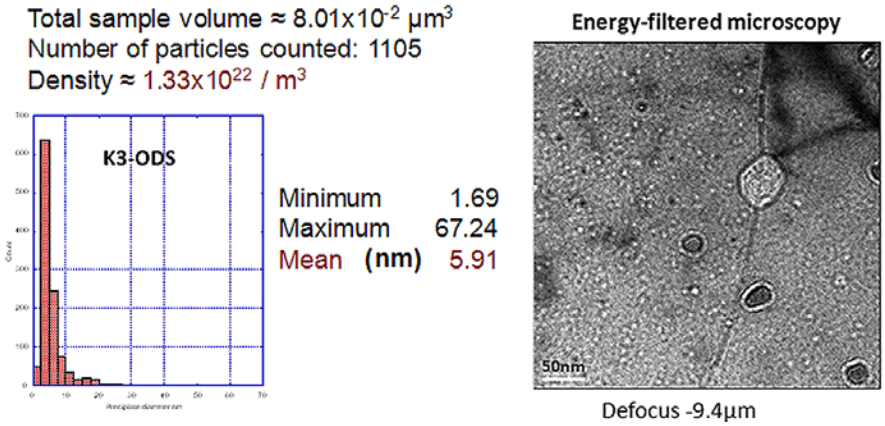

Fig. 3. The number density, the size distribution, and the mean size of oxide particles in K3-ODS steel are displayed together with a typical morphology of nanoparticles observed using energy-filtered microscopy.

Structure of oxide nanoparticles in K3-ODS steel

HRTEM studies of the structure of oxide nanoparticles and the orientation relationships between the oxide nanoparticle and the matrix were mainly conducted from K3-ODS steel samples. Since the majority of oxide nanoparticles in K3-ODS steel has a size (diameter) ranging from 1.7 nm to 30 nm according to the size distribution of oxide particles shown in Fig. 3, more attention was paid on nanoparticles smaller than 30 nm. Figure 4 shows a partially crystallized oxide nanoparticle (~7 nm in diameter) that contains a crystalline $Y_4Al_2O_9$ domain (2 nm x 5 nm in dimension). The fast Fourier transform (FFT) image generated from the crystalline $Y_4Al_2O_9$ domain is of the $[432]_{YAM}$-zone that is in agreement with the simulated $[432]_{YAM}$-zone pattern. An orientation relationship between the crystalline $Y_4Al_2O_9$ domain and the matrix is $(0\bar{1}1)_\alpha \parallel (2\bar{4}2)_{YAM}$ and $[011]_\alpha \parallel [432]_{YAM}$, which is the same as the one shown in Fig. 2. HRTEM observation of the interfacial structure between the crystalline $Y_4Al_2O_9$ domain and the matrix, as shown in Fig. 5a, reveals facets, ledges, and remnant (thin shell) of amorphous domains at the interface. Figure 5b shows the high-magnification view of an amorphous domain in the specified area in Fig. 5a. These observations clearly reveal that a solid-state amorphization of oxide nanoparticles has taken place during the MA of the ODS steel.

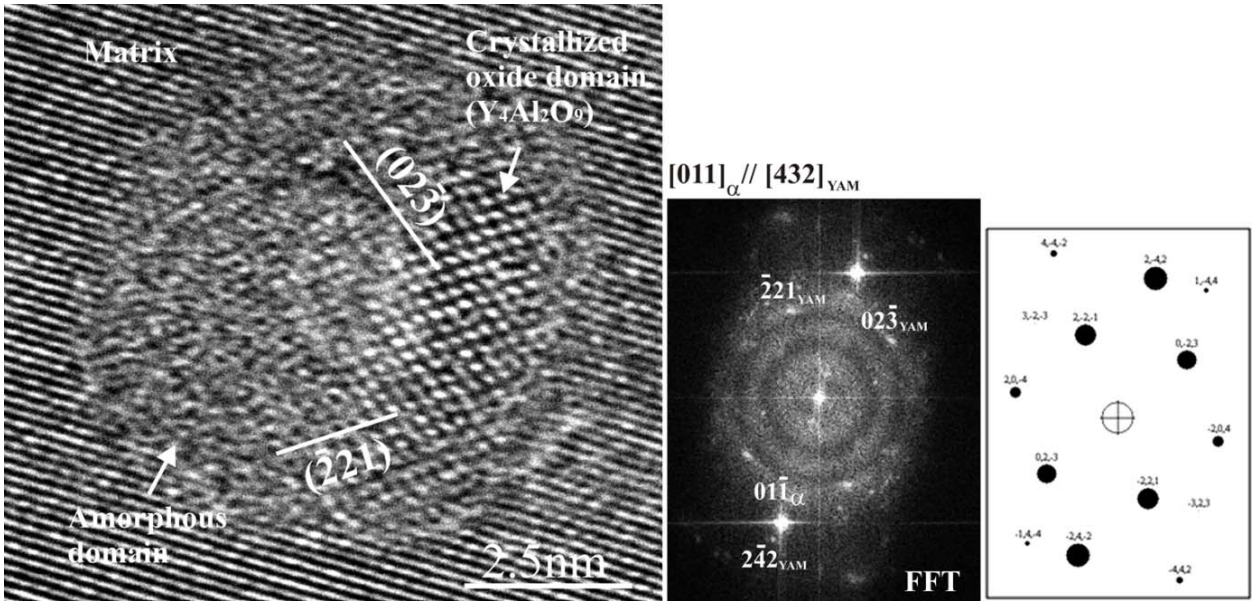

Fig. 4. HRTEM image shows a $Y_4Al_2O_9$ crystalline domain (2 x 5 nm) formed in a partially crystallized nanoparticle, and a FFT image is displayed with a simulated diffraction pattern of the $[432]_{YAM}$-zone. The orientation relationship between the crystalline domain and the matrix is the same as the one shown in Fig. 2.

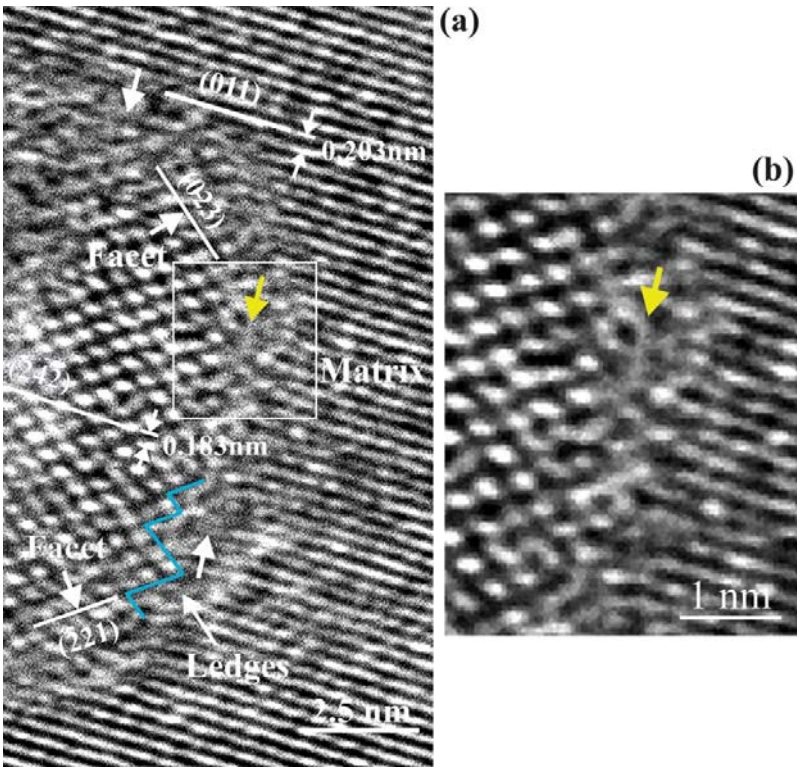

Fig. 5. HRTEM images show the structure of interface between the crystalline domain and the matrix in Fig. 4. (a) Facets, ledges, remnant of amorphous domains (marked by arrows) can be readily seen at the interfaces, and (b) a higher magnification view of an amorphous domain in a framed area in (a).

Amorphous or disordered cluster-domains smaller than 2 nm were observed using HRTEM but could not be detected using EFTEM. The result is shown in Fig. 6, in which the atomic structure of a nearly perfect matrix of the [012]-zone is shown in Fig. 6a, and the amorphous or disordered cluster-domain (marked by circles) is shown in Fig. 6b. The featureless appearance of disordered cluster-domains can be readily seen in comparison to the lattice-fringe appearance of the [012] crystalline matrix. The observations of crystalline and stoichiometric oxide nanoparticles larger than 2 nm and disordered cluster-domains smaller than 2 nm suggest that the crystallization of amorphous or disordered domains during the consolidation of the K3-ODS at 1150 °C cannot take place when the domain sizes are smaller than a critical size ($d_c \approx 2$ nm) due to the insurmountable increase of interfacial energy. To further verify and confirm that the solid-state amorphization of oxide particles does occur during MA of K3-ODS steel, another crucial observation is shown in Fig. 7, in which a $Y_4Al_2O_9$ nanoparticle of the $[311]_{YAM}$-zone is shown. The fragmentation of a powder particle presumably occurred through an ablation and/or a cleavage fracture during MA can still be recognized from a remnant of sharp and irregular particle/matrix interface. An amorphous domain (marked by arrows) remains adjacent to the re-crystallized fragment, which is no longer Y_2O_3 but $Y_4Al_2O_9$, suggesting that a solid-state amorphization does occur during MA presumably through disordering and solute mixing of Y_2O_3 particle fragments with the matrix constituents (M: Fe, Cr, Al, W, Ti), i.e., $Y_2O_3 + M \xrightarrow{disordering\ \&\ solute\ mixing} [YMO]_{amorphous}$. We believe that the results shown here strongly support the idea that during the consolidation at 1150 °C, nucleation of the crystalline complex-oxide core occurs within the large amorphous particle ($d > d_c$) by depleting Fe,

Cr, W, and Ti to the shell, i.e., $[YMO]_{amorphous} \xrightarrow{\Delta} Y_4Al_2O_9$ or $YAlO_3$ (core) + M′ (shell). The shell remains amorphous and contains a small amount of oxygen according to the APT analysis reported in [20]. It is noteworthy that the additional alloying elements can enhance amorphization of crystalline materials since the increased number of atom species can render the crystalline materials more difficult to arrange the constituent atoms into crystallized structure; for example, an amorphous phase can be obtained in ball-milled Fe-Cr powder particles in the presence of oxygen, but only a crystalline phase can be obtained in the absence of oxygen [23]. The solid-state amorphization caused by MA has accordingly been employed as one of the non-equilibrium processing routes to produce amorphous materials for many metallic and oxide systems [24].

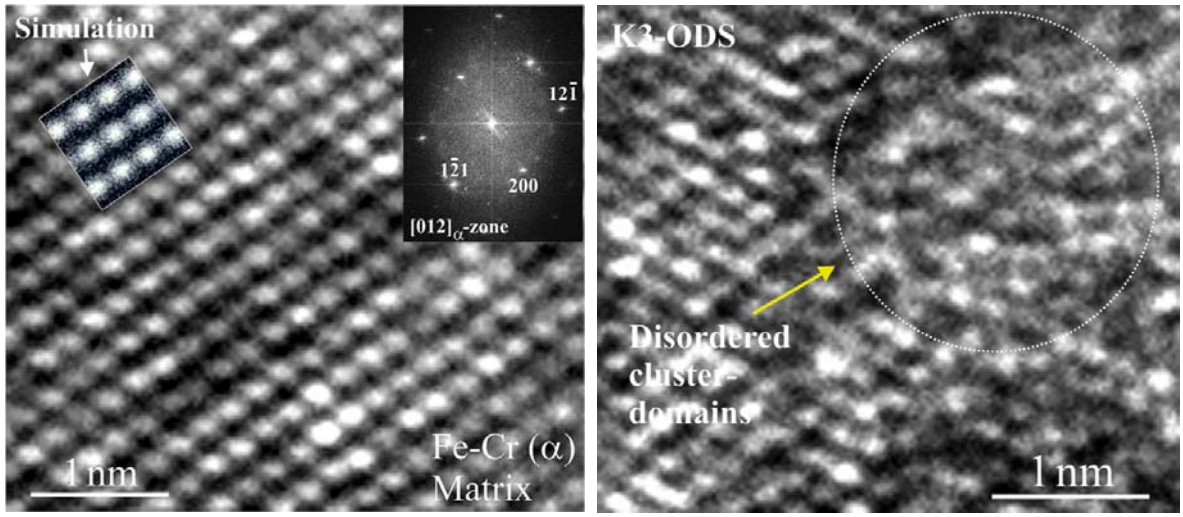

Fig. 6. HRTEM images show the atomic structure of (a) a nearly perfect matrix of the [012]-zone and (b) matrix of the [012]-zone containing a disordered cluster-domain (d < 2 nm). Notice the inset in (a) is the simulated atomic structure of the [012]-zone.

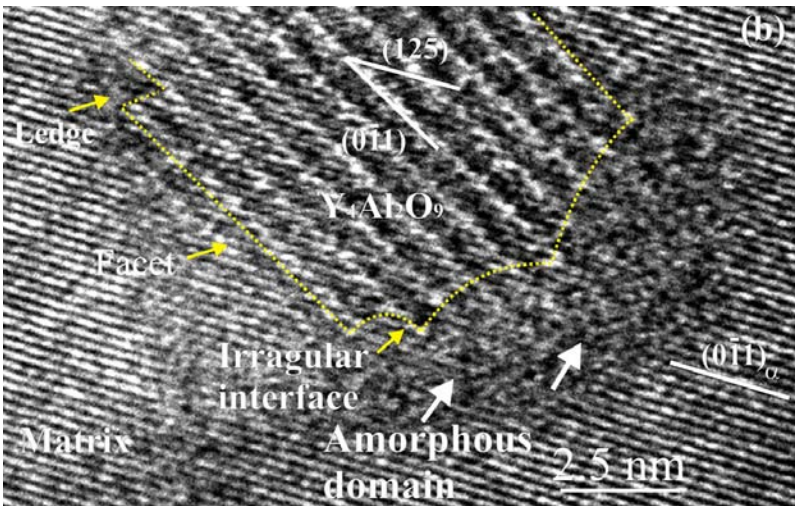

Fig. 7. HRTEM image reveals that an amorphous domain (marked by arrows) remains adjacent to the $Y_4Al_2O_9$ fragment. This observation suggests that a solid-state amorphization can occur through the mechanical attrition and chemical agglomeration of Y_2O_3 particles with matrix constituents.

The nature of cavities in (Fe^{8+} + He^{+}) dual-ion irradiated K3-ODS steel

Under steady-state conditions, the radial growth rate of helium-filled cavities is determined by both the excess vacancy flux (S) and the helium gas pressure (P_g) from the number of helium atoms (N_g) in each cavity, according to the rate theory of swelling in irradiated metals [25, 26]. The increase in both S and N_g in the high-energy neutron damage environment of fusion reactors can result in the decrease in the critical cavity radius above which rapid vacancy- or bias-driven growth occurs and leads to cavitational swelling. When the number of helium atoms within a cavity exceeds a critical value (n_g^*), the critical radius effectively disappears and bias-driven cavity growth occurs regardless of the cavity radius. The size for which the critical radius disappears upon the addition of more helium is termed the minimum critical radius (r_c^*). The helium-filled cavities with radii larger than r_c^* are called voids; the helium-filled cavities with radii smaller than r_c^* are called helium-inflated cavities or helium bubbles. It is noteworthy that theoretically the critical cavity radius containing no helium gas (r_c^0) is about 1.5 times of the critical cavity radius containing helium gas (r_c^*) [28], which has been empirically determined to be 2.5 nm (i.e., d_c^* = 5 nm) in an Fe-10 Cr alloy that was implanted with 300 ppm helium, annealed, and then ion-irradiated to 30 dpa at 574 °C [27].

A crucial concept (hypothesis) of developing ODS steels for radiation tolerance or swelling resistance is that the onset of swelling can be effectively delayed by the formation of a high-density of helium-filled cavities at a fine dispersion of nano-scale particles to reduce the number of helium atoms for each cavity to below the critical number of helium atoms (n_g^*) thus inhibiting rapid void growth. The reasons of achieving this effect can be twofold. First, an increase in cavity density leads to an increase in n_g^* and r_c^* because the excess vacancy flux (S) to each cavity is reduced. The second reason is that an increase in cavity density can reduce the accumulation rate of helium atoms in each cavity since the number of helium atoms available is diluted over a large number of cavities. Thus, the helium concentration, which can be accommodated without swelling, is greater in ODS steels than in a non-ODS matrix of the same alloy composition. A cavity number density higher than 5 x 10^{12} m^{-3} was accordingly postulated by Mansur and Lee [28] to be one of the principles for alloy design to achieve swelling resistance. According to their theoretical calculations, ~7.5 x 10^3 appm helium can be accommodated without triggering swelling when the cavity number density is 5 x 10^{12} m^{-3}. It is noteworthy that for an assumed plant lifetime of 30 years, ~ 750 dpa and ~7.5 x 10^3 appm helium will be produced in the first wall of a fusion reactor [29]. The existence of critical quantities of r_c^* and n_g^* for bubble-to-void conversion leads to the expectation of a bimodal size-distribution of cavities. That is, some cavities containing more than n_g^* helium atoms grow more rapidly to larger voids, and other cavities containing less than n_g^* helium atoms remain as small and stable bubbles. A bimodal size-distribution of cavities was accordingly observed in irradiated Fe-Cr ferritic alloys containing a low-number density (< 1 x 10^{21} m^{-3}) of oxide particles or no oxide particles [4, 27, 30], and a unimodal size-distribution of cavities was observed in irradiated ODS steels containing a high number-density (> 1x 10^{23} m^{-3}) of oxide particles [30]. To reveal the effect of nanoparticles on the distribution natures of cavities and the role nano-scale crystalline-oxide particles and amorphous clusters in trapping the helium-filled cavities, (Fe^{8+} + He^{+}) dual-ion irradiation experiments were conducted on K3-ODS steel. Effort was made to observe and image the cavities using TEM imaging techniques under out-of-focus (defocus) conditions. Cavities appear as white dots surrounded with a dark Fresnel fringe in under-focus images, and as dark dots surrounded with a bright Fresnel fringe in over-focus images [31].

A typical TEM observation of a unimodal distribution of cavities in irradiated K3-ODS is shown in Fig. 8, in which the formation of cavities in association with crystalline-oxide particles (labeled A, B, C; d ≈ 10 nm) and clusters (d < 2 nm), both can be more readily seen under an over-focus condition of +1 μm. The cavities in association with cluster-cores can have nearly spherical-, platelet-, or cuboidal-shape depending on the shapes of the clusters. Those nearly spherical cavities, which contain spherical clusters (d < 2 nm), have an apparent size: 3 nm to 4 nm in diameter. Those platelet cavities (~2.5 nm thick) contain platelet clusters that are thinner than 2 nm. Since almost all the observed cavities have sizes smaller than r_c^0 (~3.15 nm) or d_c^0 (~6.3 nm), they can be called helium-inflated cavities or helium bubbles. High-resolution TEM observations of helium bubbles formed in association with disordered cluster-domains are shown in Fig. 9. Here the helium bubbles appear as white contrast surrounded with a dark Fresnel fringe in the under-focus images. Also noted is that the helium bubble appears as a thin "shell" "encompassing" feature of helium surrounding the disordered cluster-domain.

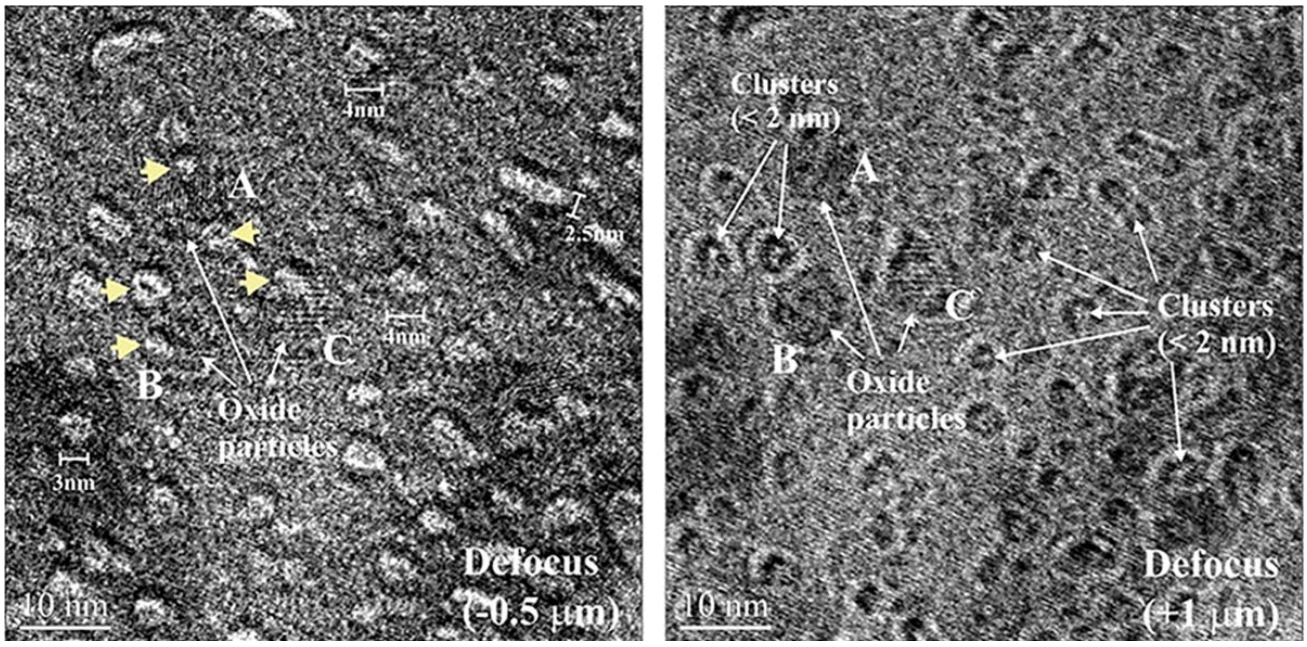

Fig. 8. TEM images show the formation of cavities in association with crystalline-oxide particles (labeled A, B, C; d ≈ 10 nm) and clusters (d < 2 nm), both can be more readily seen under an over-focus condition of +1 μm.

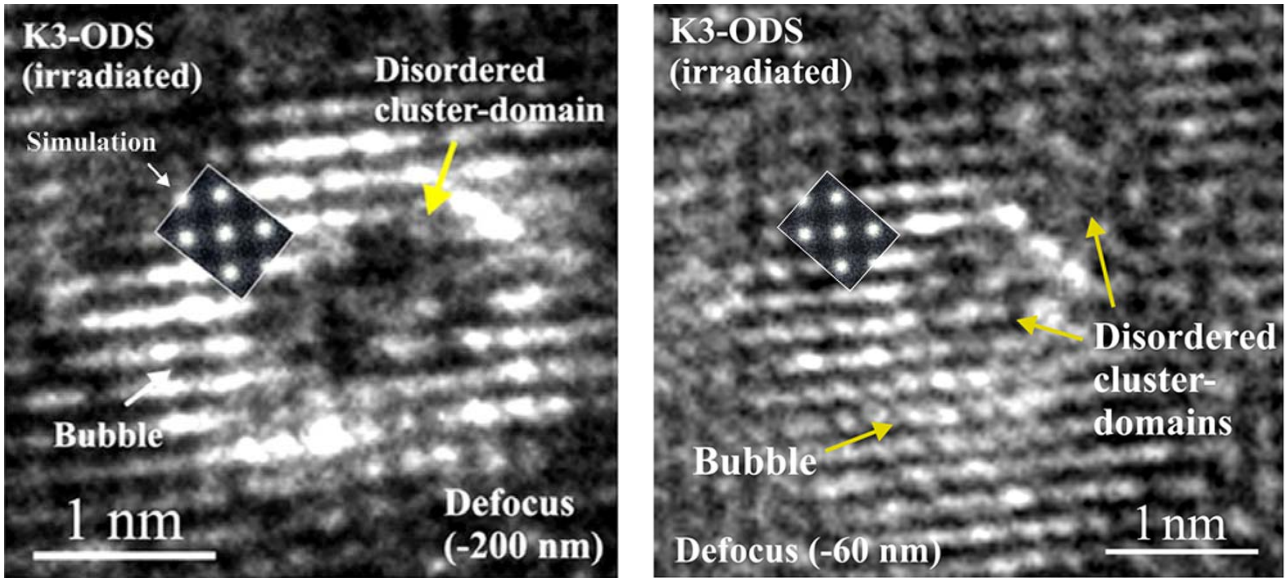

Fig. 9. HRTEM images shows that the formation of two helium bubbles in association with two different disordered cluster-domains viewing from the [001] direction, in which the helium bubbles appear as white contrast surrounded by a dark Fresnel fringe in the under-focus images. Notice the insets are the simulated atomic structure of the [001]-zone.

In summary, the cavity number density in irradiated K3-ODS is ~2.0 x 10^{23} m^{-3}, which is an order of magnitude higher than both the number density of crystalline-oxide nanoparticles of ~1.0 x 10^{22} m^{-3} (Fig. 3). This suggests that the helium-filled cavities (bubbles) in irradiated K3-ODS were mostly trapped at amorphous nanoclusters (d < 2 nm), which are difficult to resolve using conventional TEM imaging techniques. The K3-ODS steel is considered to be swelling resistant since the cavity number density in irradiated K3-ODS is greater than the critical number density of 5 x 10^{22} m^{-3} for alloy design to achieve swelling resistance [28].

CONCLUSION

The crystal structure, the number density, the size distribution, and the interfacial structure of oxide nanoparticles in Fe-16Cr-4.5Al-0.3Ti-2W-0.37Y_2O_3 (K3) ODS ferritic steels have been investigated. Oxide nanoparticles with a structure characterized by a crystalline core and an amorphous shell were frequently observed in K3-ODS steel. The core is mainly $Y_4Al_2O_9$ (YAM) complex-oxide. Small crystalline nanoparticles (d < 10 nm) tend to be coherent or semi-coherent with the matrix; large crystalline nanoparticles (d > 20 nm) tend to be incoherent with the matrix. A three-stage formation mechanism of oxide nanoparticles is proposed: (1) Fragmentation of starting Y_2O_3 particles during early stages of ball milling; (2) Agglomeration and solid-state amorphization of Y_2O_3 fragments mixing with matrix constituents during later stages of ball milling; (3) Crystallization of the amorphous agglomerates larger than ~2 nm to form oxide nanoparticles with a core/shell structure during the consolidation at 1150 °C. Agglomerates or clusters smaller than ~2 nm remain amorphous (disordered). Results of (Fe^{8+} + He^{+}) dual-ion irradiation experiments reveal the formation of a unimodal distribution of cavities with a number density of ~2 x 10^{23} m^{-3} in K3-ODS. The unimodal distribution of cavities in K3-ODS is likely due to the heterogeneous nucleation of cavities at high number density of nanoclusters (d < 2 nm).

ACKNOWLEDGEMENTS

This work was performed under the auspices of the U.S. Department of Energy by Lawrence Livermore National Laboratory under Contract DE-AC52-07NA27344. Work at LLNL was funded by the Laboratory Directed Research and Development Program at LLNL under project tracking code 09-SI-003. The author gratefully acknowledges Professor A. Kimura of Kyoto University for providing K3-ODS steel samples, M. Wall for particle-size distribution analyses, N. Teslich and R. Gross for TEM sample preparations, and B. Choi and R. Krueger for the design of sample holder for irradiation.

REFERENCES

1. K. Ehrlich, Phil. Trans. R. Soc. Lond. A 357 (1999) 595.
2. S. Ukai, M. Fujiwara, J. Nucl. Mater. 307-311 (2002) 749.
3. A. Kohyama, M. Seki, K. Abe, T. Muroga, H. Matsui, S. Jitukawa, S. Matsuda, J. Nucl. Mater. 283-287 (2000) 20.
4. I.–S Kim, J.D. Hunn, N. Hashimoto, D.L. Larson, P.J. Maziasz, K. Miyahara, E.H. Lee, J. Nucl. Mater. 280 (2000) 264.
5. T. Tanaka, K. Oka, S. Ohnuki, S. Yamashita, T. Suda, S. Watanabe, E. Wakai, J. Nucl. Mater. 329-333 (2004) 294.
6. E.E. Bloom, J. Nucl. Mater. 85-86 (1979) 795.
7. K. Yutani, H. Kishimoto, R. Kasada, A. Kimura, J. Nucl. Mater. 367-370 (2007) 423.
8. S. Uki, T. Nishida, H. Okada, T. Okuda, M. Fujiwara, K. Asabe, J. Nucl. Sci. Technol. 34 (3) (1997) 256.
9. S. Uki, T. Nishida, T. Okuda, T. Yoshitake, J. Nucl. Sci. Technol. 35 (4) (1998) 294.
10. C. Boudias, D. Monceau, The crystallographic software for research and teaching, Senlis, France (1989-1998).
11. A. Nørlund Christensen and R.G. Hazell, Acta Chemica Scandinavica 45 (1991) 226.
12. W.Y. Ching, Y.N. Xu, Physical Review B 59 (20) (1999) 12815.
13. V. de Castro, T. Leguey, M.A. Monge, A. Munoz, R. Pareja, D.R. Amador, J.M. Torralba, M. Victoria, J. Nucl. Mater. 322 (2003) 228.
14. T. Okuda, M. Fujiwara, J. Mater. Sci. Lett. 14 (1995) 1600.
15. Y. Kimura, S. Takaki, S. Suejima, R. Uemori, H. Tamehiro, ISIJ International, 39 (2) (1999) 176.
16. H. Sakasegawa, M. Tamura, S. Ohtsuka, S. Ukai, H. Tanigawa, A. Kohyama, M. Fujiwara, J. Alloys & Compounds 452 (2008) 2.
17. M.J. Alinger, G.R. Odette, D.T. Hoelzer, Acta Materialia 57 (2009) 393.
18. L.S. Darken, R.W. Gurry, Physical Chemistry of Metals, McGraw-Hill, New York 1953.
19. L. Wen, X. Sun, Z. Xiu, S. Chen, C-T Tsai, J. Europ. Ceram. Soc. 24 (2004) 2681.
20. E.A. Marquis, Appl. Phys. Lett. 93 (2008) 181904.
21. M. Klimiankou, R. Lindau, A. Möslang, J. Nucl. Mater. 386-388 (2009) 553.
22. L.L. Hsiung, M.J. Fluss, A.Kimura, Mater. Lett. 64 (2010) 1782.
23. T. Koyano, T. Takizawa, T. Fukunaga, U. Mizutani, S.Kamizuru, E. Kita, A. Tasaki, J. Appl. Phys. 73 (1993) 429.
24. C. Suryanarayana, Progress in Materials Science 46 (2001) 1.
25. L.K. Mansur, W.A. Coghlan, J. Nucl. Mater. 119 (1983) 1.
26. L.K. Mansur, E.H. Lee, P.J. Maziasz, A.P. Rowcliffe, J. of Nucl. Mater. 141-143 (1986) 633.
27. L.L. Horton, L.K. Mansur, ASTM STP 870 (1985) 344.
28. L.K. Mansur, E.H. Lee, J. of Nucl. Mater. 179-181 (1991) 105.

29. K. Ehrlich, Fusion Eng. Des. 56-57 (2001) 71.
30. T. Yamamoto, G.R. Odette, P. Miao, D.J. Edwards, R.J. Kurtz, J. of Nucl. Mater., 386-388 (2009) 338.
31. M. Ruhle, M, Wilkens, Cryst. Lattice Defects 6 (1975) 129.